High-Resolution Angular Displacement Technology Based on Varying Moiré Figure Phase Positions

Hai Yu, *Member, IEEE*, Xingdan Jia, Qiuhua Wan, Lihui Liang, and Changhai Zhao

***Abstract*— Angular displacement measurement is a popular research subject. The grating of traditional angular measurement devices uses multi-circle code and is difficult to miniaturize. This paper proposes a novel angular displacement technology based on varying moiré figure phase positions which allows for reduced volume and high-resolution angle measurements in small-size gratings. First, a moiré figure phase model is established and the calculation arithmetic is written. Second, the proposed arithmetic based on differences in moiré figure phase positions is completed accordingly. At last, a test device was fabricated based on the proposed theory with a total diameter of 35 mm and grating diameter of 25 mm. These tests show that angular displacement method based on differences of moiré figure phase positions can achieve a high resolution measurement when the diameter of calibration grating is small. We hope the results of this paper provide a workable theoretical foundation for future photographic encoders.**

***Index Terms*— Angular measurement, moiré figure, phase difference, high resolution.**

I. Introduction

HIGH-RESOLUTION and high-precision angle measurement techniques are a popular research subject [1]–[3]. It is widely used in many fields, such as radar, aerospace, robot, CNC machine tool and high precision closed-loop speed control system, because of its high precision, high resolution, wide measurement range, easy maintenance and reliable use. In aerospace, military and industrial fields, which have strict requirements on the volume and weight of devices, the requirements of photoelectric encoder not only reduce the size and weight, but also improve the resolution and precision of photoelectric encoder. At present, it is a hot research topic to improve the resolution and angle measurement accuracy of photoelectric encoder while reducing the code disk.

Development trends currently favor image detection [4]–[11] instead of traditional photoelectric conversion elements and imaging processes as opposed to moiré figures when grating size is small [12]–[15]. These techniques realize high measurement resolution, but their dynamic performance may be degraded by the frequency response of the image detector [14], [16], [17]. Moiré figures may, however, function properly under stringent frequency response and small grating size conditions while providing high-resolution measurements [18], [15].

There is a wealth of research on photoelectric encoders. The absolute encoder designed by Heidenhain Company, which has a large circular grating, can reach 27-bit resolution [19]; a likewise large and ultra-high resolution absolute encoder was designed by the Goddard Space Center as an optical pattern recognition and image processing technology. These devices measure their targets via grating calibration, where the grating is used to draw a moiré figure from which the photo electricity signal is collected by photoelectric conversion. Codes must be supplied to the grating, e.g., natural binary code, gray code, matrix code. Several circular lines are carved on the grating to ensure high measurement resolution. When the grating is small in size, however, it is very difficult to achieve high resolution.

This paper proposes a novel absolute angle measurement method which works based on differences in moiré figure phase positions. We built a moiré figure model and phase arithmetic, then developed a new angle measurement model based on varying moiré figure phase positions. We designed a Φ35-mm diameter encoder to test the proposed method and achieved resolution up to $0.62''$ with mean-square error deviation of $21.14''$. The proposed setup represents significant advantages, to this effect, over the traditional encoder.

The remainder of this paper is organized as follows: Section 2 discusses the moiré figure model. Section 3 discusses the proposed high-resolution angular displacement technology based on varying moiré figure phase positions. Section 4 presents our designed device. Section 5 explains the errors analyses. Section 6 reports our test results. Section 7 provides a brief summary and conclusion.

II. Principle of Moiré Fringes

A. Moiré Figure Model

Moiré fringe is a commonly used measurement signal. Moiré fringes can be generated by two relatively moving gratings, as shown in Figure 1.

In Figure 1, the angle between the calibrated grating and the indicating grating is α. When the calibration grating and the indicator grating are relative moving, the light passing through the grating pair forms a sinusoidal-like series of variations.

Manuscript received October 10, 2018; revised December 2, 2018; accepted December 8, 2018. Date of publication December 11, 2018; date of current version February 15, 2019. This work was supported in part by the National Natural Science Foundation of China under Grant 51605465 and in part by the Science and Technology Development Programme of Jilin Province under Grant 20180520184JH. The associate editor coordinating the review of this paper and approving it for publication was Prof. Aime Lay-Ekuakille. *(Corresponding author: Hai Yu.)*

H. Yu, Q. Wan, L. Liang, and C. Zhao are with the Changchun Institute of Optics, Fine Mechanics and Physics, Chinese Academy of Sciences, Changchun 130033, China (e-mail: yuhai@ciomp.ac.cn).

X. Jia is with the Changchun Institute of Optics, Fine Mechanics and Physics, Chinese Academy of Sciences, Changchun 130033, China, and also with the Graduate University of Chinese Academy of Sciences, Beijing 100039, China.

Digital Object Identifier 10.1109/JSEN.2018.2886309

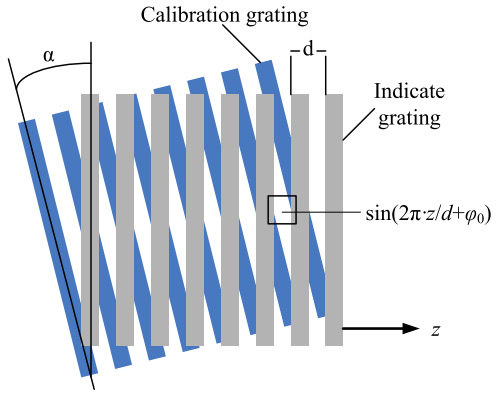

Fig. 1. Moiré fringe principle.

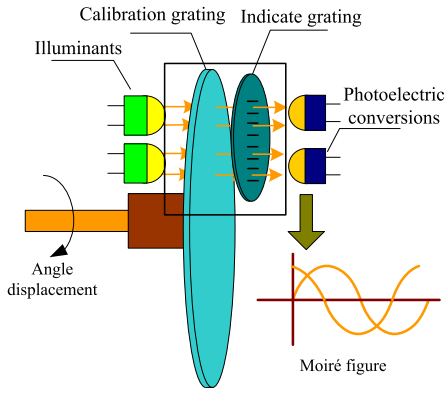

Fig. 2. Moiré figure conversion principle.

When the angle α is small, the relative displacement is z and the grating period is d. Under the illumination of the unit light, the light intensity passing through the indicator grating can be expressed as follows:

$$I = \sin(2\pi \cdot \frac{z}{d} + \varphi_0) \tag{1}$$

where φ_0 is the initial phase; 2π is the sine function period; φ_0 has different values at different locations in the indicator grating. The displacement z can be determined by measuring the sine function phase in Formula (1).

B. Phase Arithmetic

To measure the angular displacement, we installed the calibrated grating on the axis of rotation, fixed the indicator grating, and converted the moiré fringes into electrical signals by using the photosensitive elements shown in Figure 2.

The indicator grating phase shift produced $\varphi_0 = 0$, $\varphi_0 = \pi/2$, $\varphi_0 = \pi$, and $\varphi_0 = 3\pi/2$ (four channel) moiré fringe. They can be changed to electrical signals via the photoelectric conversion elements as shown in Formula (2).

$$\begin{cases} P_1 = A\sin(\omega) \\ P_2 = A\sin(\omega + \pi/2) \\ P_3 = A\sin(\omega + \pi) \\ P_4 = A\sin(\omega + 3\pi/2) \end{cases} \tag{2}$$

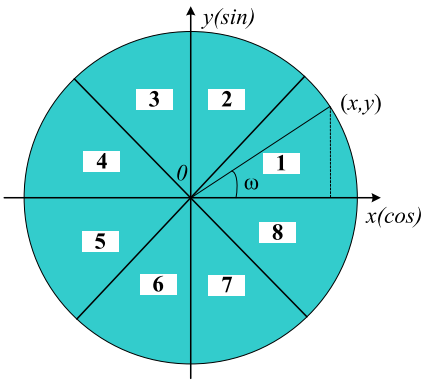

Fig. 3. Phase model in polar coordinates.

where A is the moiré signal amplitude; ω is the phase. The value of ω contains the angular displacement.

We first need to calculate the phase of Moiré fringe to achieve angular displacement measurement. The following two trigonometric functions eliminate the sensitivity to nonlinearities:

$$\begin{cases} x = P_1 - P_3 = 2A\sin(\omega) \\ y = P_2 - P_4 = 2A\cos(\omega) \end{cases} \tag{3}$$

where x, y are two electrical signals with the phase difference $\pi/2$ period. According to Formula (3), the phase can be calculated as follows:

$$\omega = atan(x/y) \tag{4}$$

The results of Formula (4) are in the range of $-\pi/2 \sim \pi/2$, so the model of Formula (4) is wrapped.

We drew two moiré signals in polar coordinates as shown in Figure 3.

The included angle ω is the phase angle of two signals. We divided an area every $\pi/4$ angle in one circle to create eight areas in total. The corresponding phase "unwrapping" arithmetic is as follows.

In area 1, $0 \le \omega < \pi/4$, $\omega = atan(x/y)$;
In area 2, $\pi/4 \le \omega < \pi/2$, $\omega = \pi/2 - atan(x/y)$;
In area 3, $\pi/2 \le \omega < 3\pi/4$, $\omega = \pi/2 + atan(-x/y)$;
In area 4, $3\pi/4 \le \omega < \pi$, $\omega = \pi - atan(y/-x)$;
In area 5, $\pi \le \omega < 5\pi/4$, $\omega = \pi + atan(-y/-x)$;
In area 6, $5\pi/4 \le \omega < 3\pi/2$, $\omega = 3\pi/2 - atan(-x/-y)$;
In area 7, $3\pi/2 \le \omega < 7\pi/4$, $\omega = 3\pi/2 + atan(x/-y)$;
In area 8, $7\pi/4 \le \omega < 2\pi$, $\omega = 2\pi - atan(-y/x)$.
Which yields the "unwrapping" phase-values ω.

III. Principle of Varying Moire Fiprinciple of Moiré Fringe Phase Positions

A. Varying Moiré Figure Phase Model

Rotating the grating around produces an abundance of periodic moiré fringe signals. The absolute angular position information cannot be obtained by focusing on solely one channel phase fringe signal.

For absolute angle measurement, we marked three circles of grating lines on the calibrated grating. The three channels are S1, S2, and S3. S1 has 2^n grate lines, S2 has $2^n - 1$ grate

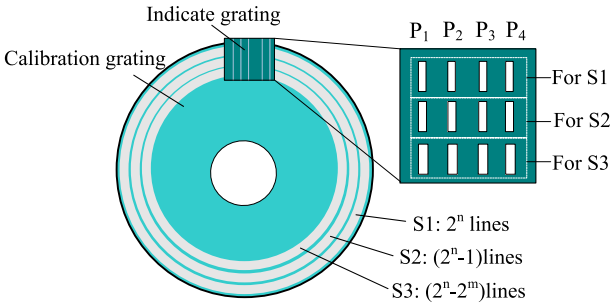

Fig. 4. Grating pattern.

lines, and S3 has $2^n - 2^m$ grate lines. The grating pattern is shown in Figure 4. There are four lines for each circle in the indicator grating which provide four signals ($P_1 \sim P_4$) of each channel moiré fringe, such as Formula (4).

The grating periods of S1, S2, and S3 are $d_1 = 360/2^n$, $d_2 = 360/(2^n - 1)$, and $d_3 = 360/(2^n - 2^m)$. When the measured angle displacement is θ, it can be plugged into Formula (2) and Formula (3) to determine the moiré fringe electrical signals of S1, S2, and S3 as (x_1, y_1), (x_2, y_2), and (x_3, y_4).

The moiré fringe signals for circle S1 are determined as follows:

$$\begin{cases} x_1 = A\sin(\omega_1) = A\sin(2\pi \cdot \dfrac{\theta}{360/2^n}) \\ y_1 = A\cos(\omega_1) = A\sin(2\pi \cdot \dfrac{\theta}{360/2^n} + \pi/2) \end{cases} \tag{5}$$

For the S2 circle, the moiré fringe signals are as follows:

$$\begin{cases} x_2 = A\sin(\omega_2) = A\sin[2\pi \cdot \dfrac{\theta}{360/(2^n - 1)}] \\ y_2 = A\cos(\omega_2) = A\sin[2\pi \cdot \dfrac{\theta}{360/(2^n - 1)} + \pi/2] \end{cases} \tag{6}$$

and for the S3 circle:

$$\begin{cases} x_3 = A\sin(\omega_3) = A\sin[2\pi \cdot \dfrac{\theta}{360/(2^n - 2^m)}] \\ y_3 = A\cos(\omega_3) = A\sin[2\pi \cdot \dfrac{\theta}{360/(2^n - 2^m)} + \pi/2] \end{cases} \tag{7}$$

where ω_1, ω_2, ω_3 are phases of the three channel moiré fringe signals, respectively; θ is current angle displacement; 360 is the angle of one circle.

The phase ω_1, ω_2, ω_3 can be calculated as follows:

$$\omega_1 = 2\pi \cdot 2^n \cdot \frac{\theta}{360} = actan(\frac{x_1}{y_1}) \tag{8}$$

$$\omega_2 = 2\pi \cdot (2^n - 1) \cdot \frac{\theta}{360} = actan(\frac{x_2}{y_2}) \tag{9}$$

$$\omega_3 = 2\pi \cdot (2^n - 2^m) \cdot \frac{\theta}{360} = actan(\frac{x_3}{y_3}) \tag{10}$$

The absolute angular position information can be calculated from the differences of ω_1, ω_2, ω_3. So, the difference in ω_1 and ω_2 are normalized:

$$\Delta_1(\theta) = \frac{\omega_1 - \omega_2}{2\pi} = \frac{\theta}{360} \tag{11}$$

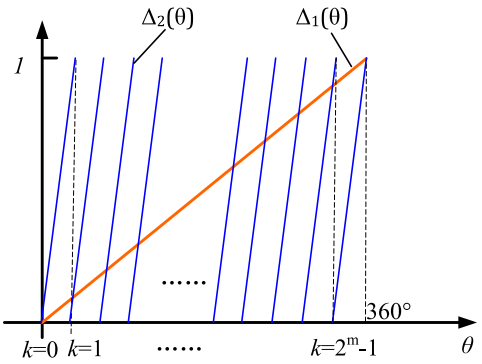

Fig. 5. Curves of $\Delta_1(\theta)$ and $\Delta_2(\theta)$.

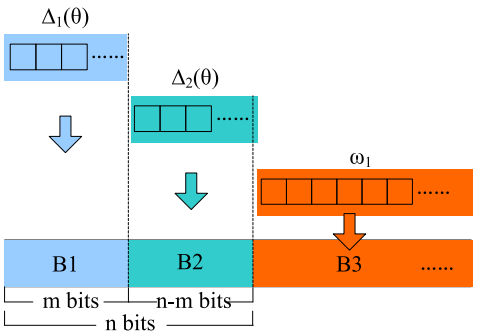

Fig. 6. Data combination.

as is the difference in ω_1 and ω_3:

$$\Delta_2(\theta) = \frac{\omega_1 - \omega_3}{2\pi} = \frac{\theta}{360/2^m} - k, \quad k = 0, 1, ..., 2^m - 1 \tag{12}$$

where k is the periodic number of $\Delta_2(\theta)$.

From Formula (11) and Formula (12), $\Delta_1(\theta)$ is directly proportional to θ and the period of $\Delta_1(\theta)$ is one circle. The period of $\Delta_2(\theta)$ is $360/2^m$, as shown in Figure 5. The period of $\Delta_2(\theta)$ is 2^m times that of $\Delta_1(\theta)$.

By $\Delta_1(\theta)$, the absolute angular measurement is complete. In practice, however, the results of ω_1 and ω_2 are affected by many factors. The value of $\Delta_1(\theta)$ contains a certain error jitter, so the resolution of $\Delta_1(\theta)$ is inherently low. Here, we use $\Delta_2(\theta)$ as the low-bit part of the angle values to enhance the measurement resolution.

B. Arithmetic of Data Linkage

Formulas (11) and (12) indicate that the frequency of $\Delta_1(\theta)$ and $\Delta_2(\theta)$ are 1 and 2^m in one circle. According to this periodic relationship, after $\Delta_2(\theta)$ changes by one circle, $\Delta_1(\theta)$ changes one bit. Similarly, when ω_1 changes by one circle, $\Delta_2(\theta)$ changes one bit. We linked the data accordingly as shown in Figure 6.

For binary calculation, we multiplied $\Delta_1(\theta)$ by 2^m and $\Delta_2(\theta)$ by 2^{n-m} as follows:

$$B_1 = 2^m \cdot \Delta_1(\theta) \tag{13}$$

$$B_2 = 2^{n-m} \cdot \Delta_2(\theta) \tag{14}$$

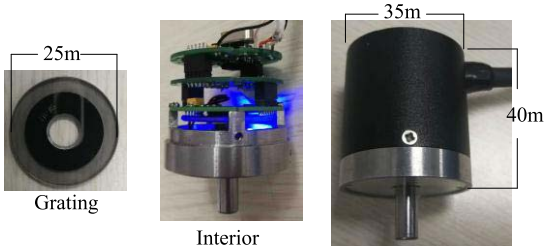

Fig. 7. Test device.

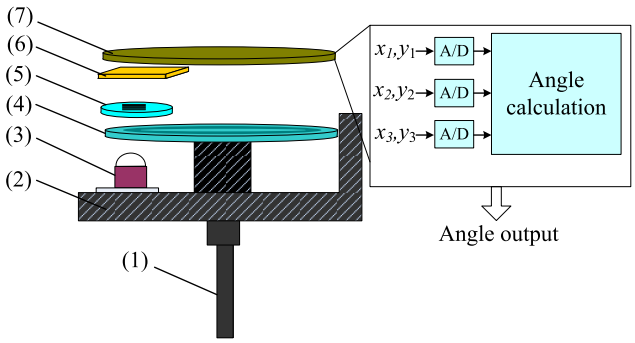

Fig. 8. Principle of designed device. (1) spindle, (2) flange, (3) parallel light, (4) calibration grating, (5) indicator grating, (6) photoelectric conversion array, and (7) circuit.

Then to increase the resolution, we placed ω_1 in the last portion of the data and multiplied ω_1 by 2^{N}:

$$B_3 = 2^N \cdot \frac{\omega_1}{2\pi} \tag{15}$$

We then obtained quantified data by B1, B2, and B3. B1 is a high m-bit, B2 is a middle (n-m)-bit, and B3 is a low N-bit. The measured angle value θ can be written in binary form as follows:

$$\theta_{\mathrm{bin}} = B_1 \cdot 2^{n-m+N} + B_2 \cdot 2^N + B_3 \tag{16}$$

The resolution is $m + (n - m) + N = n + N$ bits.

IV. Angle Measurement Device Design

We designed a test device as shown in Figure 7. It has overall diameter of 35 mm, length of 40 mm, and grating diameter of 25 mm.

The principle of designed device is shown in Figure 8. The figure includes: (1) spindle, (2) flange, (3) parallel light, (4) calibration grating, (5) indicator grating, (6) photoelectric conversion array, and (7) circuit components. The parallel light through the calibration grating and the indicator grating generates three-channel Moiré fringe signals. The photoelectric conversion array then converts the three Moiré fringes into electrical signals. In the circuit, the A/D conversions convert the three-channel signals to digital signals, respectively, and calculate the absolute angle value θ.

A. Light Design

To ensure the purity of the Moiré fringe signal, we used an optical lens to converge the light source and thus form a parallel light source (Figure 9). The point light source is a 460 nm LED and the lens focal length is 5 mm.

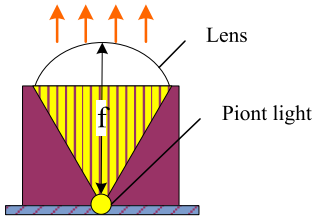

Fig. 9. Parallel light source.

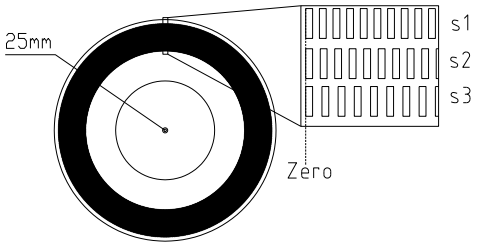

Fig. 10. Grating pattern.

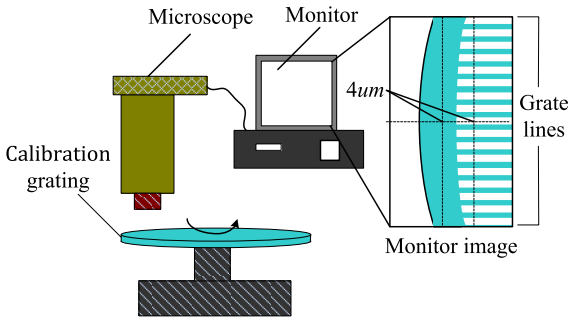

Fig. 11. Calibration grating adjustment.

B. Calibration Grating Design

We designed three codes on our grating. According to Section 3.1, we let the cycles of *S1*, *S2*, and *S3* be $2^{\mathrm{n}} = 2^{10}$, $2^{\mathrm{n}} - 1 = 2^{10} - 1$, and $2^{\mathrm{n}} - 2^{\mathrm{m}} = 2^{10} - 2^5$. The diameter of designed grating is 25cm as shown in Figure 10 with "Zero" as shown in the magnified inset. We designed the pattern by using CAD software, and the photocopy the pattern to glass. The error of marking position is less than 0.01μm.

C. Calibration Grating Adjustment

The installation of the calibration grating directly affects the accuracy of the angular displacement measurement. When designing the designed device, we used a microscope to observe the grate lines on the grating. The process is shown in Figure 11.

We observed grate line images via the microscope which allowed us to ensure all the grate lines have the same radius. Through debugging, when the grating is rotated for one circle, all the grate line radii have errors below $4\mu m$.

The indicator grating was installed very near to the calibration grating to reduce the influence of light diffraction. The parallel light source was designed to illuminate the grating pairs immediately upon start-up.

D. Device Resolution

In our design, m=5-bit and n =10-bit. In the quantification of ω_1, we quantified 2^8 data in every area shown in Figure 2. There are $8=2^3$ areas altogether, so we achieved $2^N=2^{8+3}=2^{11}$ quantification of ω_1. According to Formula (16), the resolution of our designed device is (n+N=10+11) 21-bit.

E. Response Frequency

Maximum response frequency is an important parameter of angle measurement. In our designed device, there are 3(moiré fringe channel)×2(signals) A/D conversions. Each A/D cost 10μs to complete a single conversion. The angle calculation arithmetic costs 200μs, so the maximum response frequency of designed device is $1/(6\times10\mu s+200\mu s)=3.85$kHz. This frequency is high enough for most practical applications, but could be increased by installing high performance electronic components.

V. Errors Analysis

According to previous studies, the error of angular displacement mainly includes long period errors and short period errors [20].

A. Long-Period Errors

The long period error is mainly caused by the eccentricity of the grating. Set the radius of the grating used be r, the distance between the center of the circle and the center of rotation be e, and the angle between the deviation direction and the zero position measured by the angle be $\Delta\theta$. The error caused by the eccentricity of the grating can be expressed as

$$\mu_1 = \arctan\left(\frac{e\cdot\sin\Delta\theta}{r-e\cdot\sin\Delta\theta}\right)\cdot\frac{180^\circ}{\pi} \tag{17}$$

It can be seen that when the larger grating is used, the error caused by eccentricity can be effectively reduced.

B. Short-Period Errors

The short period error is mainly caused by the deviation of the amplitude and phase of the electric signals such as Moiré fringe. The short period error is composed of multiple harmonic components, which can be expressed as

$$\mu_2 = U_1\sin(\omega+\beta_1)+U_2 \times \sin(2\omega+\beta_2)+U_3\sin(3\omega+\beta_3)+.... \tag{18}$$

In the formula (18), ω is the angle values, U_1, U_2 and U_3 are the amplitudes of each harmonic, $\beta_1, \beta_2, \beta_3$ are the phase of each harmonic.

In order to eliminate the error in Eq. (18), we adjust the amplitude and phase of the Moiré fringe signal to an approximate ideal condition.

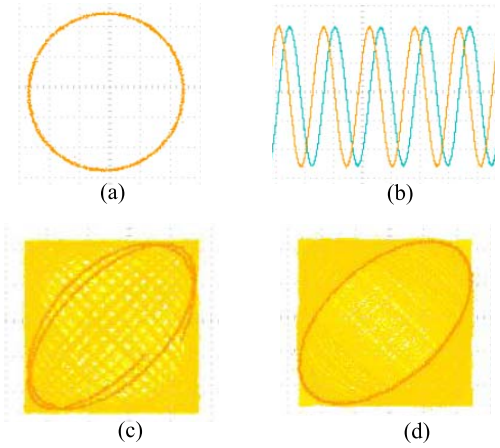

Fig. 12. The results of signal test.

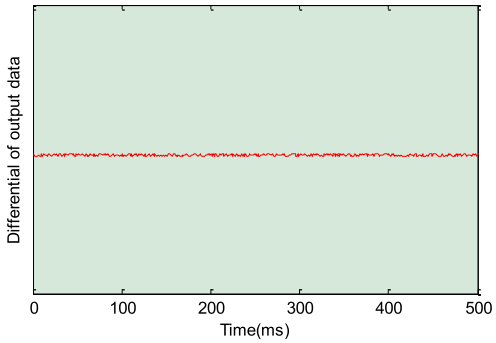

Fig. 13. Differentials of output data.

VI. Experiments

A. Signal Test

We collect signals of x_1 and y_1 as shown in figure 12(a) and figure 12(b). The phase difference is $\pi/4$, so the Lissajous in figure12(a) is roundness. By metering, the range of noise in signal is 24mV, the range of signal is 3V, so the signal noise ratio is 10log(16/0.024)=20.97dB. This value is suited for angle measurement.

The Lissajous between x_1 and x_2 is shown in figure 12(c) and Lissajous between x_1 and x_3 is shown in figure 12(d). After one circular rotation of the axis, the phase difference between x_1 and x_2 has changed from 0 to 2π for one period, the phase difference between x_1 and x_3 has changed from 0 to 2π for one period.

These results in figure 12 fit the principle in section III.

B. Resolution Test

We revolved the designed device with a servo motor at a uniform and slow speed and calculated the differentials of the output data (Figure 13). All differential data was steady when the device rotated at a uniform speed, which indicates that all the 21-bits are exact. In effect, the proposed device exhibited higher resolution than traditional small-size encoders (not higher than 18-bit).

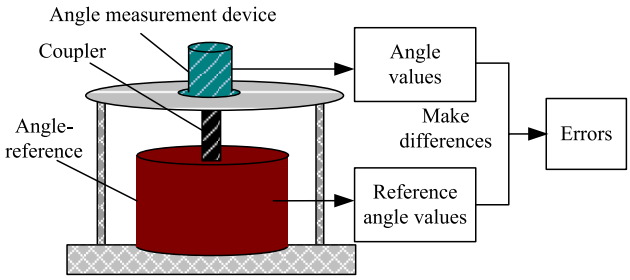

Fig. 14. Principle precision test.

TABLE I
ERROR DETECTION

Angle position	Errors	Angle position	Errors
0°	0"	195°	-32.5"
15°	6"	210°	-42.5"
30°	10. 5"	225°	-46.5"
45°	14"	240°	-43.5"
60°	13.5"	255°	-39.5"
75°	14"	270°	-31.5"
90°	14"	285°	-26"
105°	7.5"	300°	-18"
120°	3"	315°	-11"
135°	-3"	330°	-2"
150°	-13.5"	345°	-1"
165°	-18.5"	360°	0"
180°	-23"		

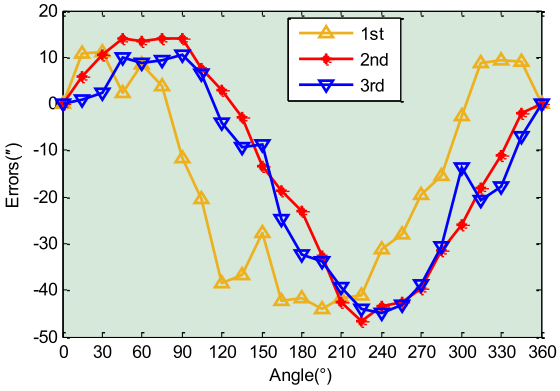

Fig. 15. Three-time tests.

C. Precision Test

We measured the proposed device by an angle-reference with precision of $2''$ and resolution of $0.07''$. We recorded the output data of both the designed device and angle-reference at each 15° point. The error was calculated according to differences values between the two devices as shown in Figure 14 and Table 1.

As shown in Table 1, we obtained a mean-square error deviation of $21.14''$. We ran three separate detection experiments as shown in Figure 15. The maximum error was $15''$ and minimum error was $-45''$. These results indicate that the proposed device has excellent precision.

D. Error Analysis

According to Section V, we analyze the errors in figure 15 as follow:

The short-period errors are very small. It explains that the Moiré figure is approximate ideal condition.

Meanwhile, we can find long-period errors obviously which looks like a sine curve. According to formulate (17), we can calculate the eccentricity value is about $e = 3.3\mu$m.

E. Uncertainty Test

In precision test, the main factors affecting the calibration results include quantization error δ_1, coaxial connection error δ_2 and angle reference error δ_3.

Quantization error is caused by the resolution of the device under test. The resolution of the angular measuring device designed by us is $0.62''$, so $\delta_1 = 0.62''$.

The coaxial connection error is mainly caused by the different axes when the measured device is connected with the angle reference through the coupling. When we calibrate, we use micrometer to measure coaxial error, the average value is 0.001 mm. It has little influence on calibration, generally no more than $2''$. So $\delta_2 = 2''$.

The error of the angle reference is the precision of the reference encoder, so $\delta_3 = 2''$.

The uncertainty of precision test is $(0.62^2+2^2+2^2)^{1//2} = 2.9''$. The mean square error of our device is $21.14''$, so by analyzing, the uncertainty of the proposed device is $(0.62^2 + 2^2+ 2^2 + 21.14^2)^{1/2} = 21.34''$.

VII. CONCLUSIONS

At present, the research of angular displacement measurement technology is developing towards smaller, higher precision and higher resolution. While miniaturizing angular displacement measurement, ensuring reliability is also a very important research content. In the future, miniaturization, high resolution and high reliability angular displacement measurement technology will be more mature and applied in various industries.

This paper proposed a high-resolution angular displacement method based on differences in moiré figure phase positions. We first built moiré figure model and corresponding phase arithmetic. We then established an angle measurement model based on varying moiré figure phase positions.

To validate the feasibility and effectiveness of our method, we designed a Φ35-mm diameter encoder. The measurement resolution in the test represents a significant advantage over traditional measurement techniques. These tests show that angular displacement method based on differences of moiré figure phase positions can achieve a high resolution measurement when the diameter of calibration grating is small. The results presented here may provide a theoretical and technological foundation for further research on small-size, high-resolution photographic rotary encoders.

REFERENCES

[1] F. Deng, J. Chen, Y. Wang, and K. Gong, "Measurement and calibration method for an optical encoder based on adaptive differential evolution-Fourier neural networks," *Meas. Sci. Technol.*, vol. 24, no. 5, p. 055007, 2013.

[2] G. Ye, H. Liu, Y. Ban, Y. Shi, L. Yin, and B. Lu, "Development of a reflective optical encoder with submicron accuracy," *Opt. Commun.*, vol. 411, pp. 126–132, Mar. 2018.

[3] C.-F. Kao, H.-L. Huang, and S.-H. Lu, "Optical encoder based on Fractional-Talbot effect using two-dimensional phase grating," *Opt. Commun.*, vol. 283, no. 9, pp. 1950–1955, 2010.

[4] V. Bianco *et al.*, "Strategies for reducing speckle noise in digital holography," *Light, Sci. Appl.*, vol. 7, Aug. 2018, Art. no. 48.

[5] G. Wang, L. Zhang, C. Wang, Z. Yan, and L. Yang, "Improved resolution optical time stretch imaging based on high efficiency in-fiber diffraction," *Light, Sci. Appl.*, vol. 8, Jan. 2018, Art. no. 600.

[6] Y. Rivenson, Y. Zhang, H. Günaydin, D. Teng, and A. Ozcan, "Phase recovery and holographic image reconstruction using deep learning in neural networks," *Light, Sci. Appl.*, vol. 7, p. 17141, Feb. 2018.

[7] F. Y. Yue *et al.*, "High-resolution grayscale image hidden in a laser beam," *Light, Sci. Appl.*, vol. 7, p. 17129, Jan. 2018.

[8] J. Qin, R. M. Silver, B. M. Barnes, H. Zhou, R. G. Dixson, and M.-A. Henn, "Deep subwavelength nanometric image reconstruction using Fourier domain optical normalization," *Light, Sci. Appl.*, vol. 5, p. e16038, Feb. 2016.

[9] W. Luo, Y. Zhang, A. Feizi, Z. Göröcs, and A. Ozcan, "Pixel super-resolution using wavelength scanning," *Light, Sci. Appl.*, vol. 5, p. e16060, Apr. 2016.

[10] A. C. Sobieranski *et al.*, "Portable lensless wide-field microscopy imaging platform based on digital inline holography and multi-frame pixel super-resolution," *Light, Sci. Appl.*, vol. 5, p. e346, Oct. 2015.

[11] S. Witte, V. T. Tenner, D. W. E. Noom, and K. S. E. Eikema, "Lensless diffractive imaging with ultra-broadband table-top sources: from infrared to extreme-ultraviolet wavelengths," *Light, Sci. Appl.*, vol. 3, p. e163, Mar. 2014.

[12] J. S. Bajić, D. Z. Stupar, B. M. Dakic, M. B. Živanov, and L. F. Nagy, "An absolute rotary position sensor based on cylindrical coordinate color space transformation," *Sens. Actuators A, Phys.*, vol. 213, pp. 27–34, Jul. 2014.

[13] Y. Sugiyama *et al.*, "A 3.2 kHz, 14-bit optical absolute rotary encoder with a CMOS profile sensor," *IEEE Sensors J.*, vol. 8, no. 8, pp. 1430–1436, Aug. 2008.

[14] M. Tresanchez, T. Pallejà, M. Teixidó, and J. Palacín, "Using the image acquisition capabilities of the optical mouse sensor to build an absolute rotary encoder," *Sens. Actuators A, Phys.*, vol. 157, pp. 161–167, Jan. 2010.

[15] J.-A. Kim, J. W. Kim, C.-S. Kang, J. Jin, and T. B. Eom, "Absolute angle measurement using a phase-encoded binary graduated disk," *Measurement*, vol. 80, pp. 288–293, Feb. 2016.

[16] H. Yu, Q. Wan, X. Lu, Y. Du, and S. Yang, "Small-size, high-resolution angular displacement measurement technology based on an imaging detector," *Appl. Opt.*, vol. 56, no. 3, pp. 755–760, 2017.

[17] H. Yu, Q. Wan, X. Lu, C. Zhao, and Y. Du, "A robust sub-pixel sub-division algorithm for image-type angular displacement measurement," *Opt. Laser. Eng*, vol. 100, pp. 234–238, Jan. 2018.

[18] J.-H. Song, K. C. Kim, and S. H. Kim, "Reducing tilt errors in moiré linear encoders using phase-modulated grating," *Rev. Sci. Instrum.*, vol. 71, no. 6, pp. 2296–2300, 2000.

[19] D. Mancini, E. Cascone, and P. Schipani, "Galileo high-resolution encoder system," *Proc. SPIE*, vol. 3112, pp. 328–334, Sep. 1997.

[20] H. Yu, Q. Wan, X. Lu, Y. Du, and C. Zhao, "Error-correct arithmetic for angular displacement measurement with single linear image detector," *Opt. Eng.*, vol. 57, no. 5, p. 054108, 2018.

Hai Yu (M'87) received the Ph.D. degree from the Changchun Institute of Optics, Fine Mechanics and Physics (CIOMP), Chinese Academy of Sciences, in 2014. He is currently an Assistant Research Fellow with CIOMP, Chinese Academy of Sciences. His research interest has been in the area of electro-optical displacement precision measurement.

Xingdan Jia was born in 1992. She received the bachelor's degree from the University of Electronic Science and Technology in 2015. She is currently a doctoral student with the University of Chinese Academy of Sciences. Her research interest has been in the area of electro-optical displacement precision measurement.

Qiuhua Wan was born in 1962. She is currently a Research Fellow with CIOMP, Chinese Academy of Sciences. Her research interest has been in the area of electro-optical displacement precision measurement.

Lihui Liang was born in 1980. He is currently an Associate Research Fellow with CIOMP, Chinese Academy of Sciences. His research interest has been in the area of electro-optical displacement precision measurement.

Changhai Zhao was born in 1980. He is currently an Associate Research Fellow with CIOMP, Chinese Academy of Sciences. His research interest has been in the area of electro-optical displacement precision measurement.